PAPER

Check for updates

Novel process for high value utilization of high-alumina fly ash: valuable metals recovery and mesoporous silica *in situ* preparation†

Jian-ming Gao, [iD] * Zhenwei Yan, Shujia Ma and Yanxia Guo*

Extraction of valuable metals besides silica from high-alumina fly ash is one of the most important high-value utilization pathways. However, it is difficult to realize high-efficiency extraction due to the stable structure *e.g.* of quartz and mullite. In this paper, mineral phase transformation for valuable metal recovery and mesoporous silica *in situ* preparation from fly ash by a selective acid leaching method was proposed. The mineral phase transformation, dissolution behavior of each metal, and pore structure of fly ash derived mesoporous silica were systematically investigated. The results show that the co-activation of fly ash by Na_2CO_3–K_2CO_3 formed the phases of kalsilite and $(Na, K)AlSiO_4$. During the acid leaching process, Al, Li, and Ga could be leached with the efficiencies of 86.17%, 89%, and 80% in the FK system. In the FN system, the efficiencies of Al, Li, and Ga are 92.38%, 95%, and 83%, respectively. The crystal plane (002) was destroyed for kaliophilite while all the crystal planes were destroyed for nepheline. With the increase of HCl solution concentration, the porous silica exhibited the same change order of pore shape. The pore structure of as-prepared porous silica was type IV and the hysteresis loop was type H3, and the specific surface areas could be 565.54, 448.02, and 746.76 m^2 g^{-1}, respectively. Finally, the leaching liquors can be used to produce crystal aluminum chloride, lithium carbonate and gallium. This paper might provide technical support for full recycling of high-value resources from fly ash.

Introduction

The generation of coal fly ash is increasing year by year, and the stockpile is about 1.4 billion tons,[1] which not only occupies the land, but also has an impact on the environment.[2,3] For many years, much effort has been committed to research on the disposal and resource utilization of fly ash, including the utilization of building materials,[4] agriculture[5] and so on, which are mainly extensive low-value utilization. Due to the special paleo-geological structure, there are huge reserves of high-alumina coal in northern Shanxi and western Inner Mongolia, associated with rare elements such as lithium (Li), gallium (Ga) and REE, *etc.* During the combustion process, these elements are further enriched in fly ash. The content of alumina[6] and silica is more than 80%, of which the mass fraction of alumina can reach 35–50 wt%, the grade of associated element Li can reach 200–400 ppm, and the grade of Ga[7] is 50–100 ppm, which is of great value for extraction of valuable elements.

Due to the stable mineral phases of mullite and quartz contained in the fly ash,[8,9] it is difficult to extract Al, Si and other

Institute of Resources and Environment Engineering, State Environmental Protection Key Laboratory of Efficient Utilization Technology of Coal Waste Resources, Shanxi University, Taiyuan 030006, P. R. China. E-mail: gaojianming@sxu.edu.cn

resources efficiently.[10] So far, several processes have been reported to extract valuable metals from coal fly ash, including the soda-lime sintering process,[11,12] ammonium sulfate sintering process,[13] alkaline leaching[14] and acid leaching process,[15] *etc.* Metallurgical grade alumina could be produced by soda-lime sintering process, which has the disadvantages of high-energy consumption and large slag discharge. Alumina and silicon could be separated efficiently from coal fly ash by the ammonium sulfate sintering process; however, the consumption of ammonium sulfate is large. Among these processes, alumina and silica could be separated efficiently from coal fly ash by the acid leaching process. About 90% of alumina could be leached from coal fly ash by the sulfuric acid pressure leaching process with the leaching temperature of 250 °C and pressure of 4.0 MPa.[16] The high investment cost as well as harsh reaction conditions limited the industrial application. How to realize the efficient separation and comprehensive utilization of valuable metals from coal fly ash in mild conditions is of great significance.

Mesoporous silica materials are widely used in catalysis, adsorption,[17–19] heat and energy storage, biomedicine and other fields because of their large specific surface, rich pore structure, easy modification, good stability, and strong biocompatibility.[20] At present, mesoporous silica materials are mainly prepared by sol–gel processes and template methods.[21] However, the biggest problem of these methods is that the precursor composition

and sol homogeneity are difficult to control, and it is difficult to achieve large-scale industrial applications.[22,23] Fly ash contains a large amount of SiO_2 and is a potential raw material for preparation of porous silica materials.[24] The typical process for synthesis of mesoporous silica using fly ash as raw material is based on alkali leaching or alkali fusion. The sodium silicate solution obtained by solid–liquid separation is used as a silicon source. After repeated extraction and impurity removal, ordered mesoporous silica is obtained by sol–gel[25] or template methods. Due to stable mineral phases of mullite, quartz and others in fly ash, the utilization efficiency of SiO_2 is low, only 30–50%. Furthermore, the expensive template and time consumption for sol–gel process limit the application of fly ash derived mesoporous silica.

In the previous work, alumina could be efficiently leached from coal fly ash by an atmospheric acid leaching process after mineral transformation of stable mullite and quartz into nepheline.[6] There is no further study on pore structure regulation and the pore forming mechanism of silica materials. Furthermore, the crystalline structure of nepheline and kaliophilite would be different under different reaction conditions, which could inevitably lead to the difference of metal leaching behaviors and pore structure of silica materials. In this paper, mineral phase transformation for *in situ* preparation mesoporous silica materials and valuable metal recovery from fly ash by selective acid leaching method was proposed, the dissolution behavior of Al, Li, Ga, Si *etc.* and the mechanism of pore structure formation from nepheline and kaliophilite crystals in the process of acid leaching will be systematically studied, and the pore structure regulation of fly ash derived mesoporous silica materials will be revealed, providing the theoretical basis and technical support for comprehensive utilization of Al, Li, Ga, Si *etc.* in fly ash to prepare high value-added materials.

Experimental

Materials

The fly ash (FA) was provided by Datang Power Generation Co., Ltd. The chemical compositions of FA were shown in Table 1. The content of SiO_2 and Al_2O_3 is 45.63% and 43.88%, respectively, and the grades of Li and Ga reach 252 and 68 ppm, respectively. Sodium carbonate (Na_2CO_3), potassium carbonate (K_2CO_3) and hydrochloric acid (HCl) are in analytical grade, which were purchased from Sinopharm Chemical Reagent Co., Ltd, and used without any pretreatment.

Experimental procedure

Mineral phase transformation process. The mineral phase transformation for FA was conducted in muffle furnace. FA was dried first and then mixed with Na_2CO_3 and/or K_2CO_3 respectively *via* a planetary ball mill for 2 h. The sample was calcined

in the muffle furnace at the designed temperature for 2 h and cooled to room temperature to obtain activated fly ash. To study the effect of alkali metal cations on the mineral phase transformation for fly ash, three systems including fly ash–sodium carbonate (FN), fly ash–potassium carbonate (FK) and fly ash–sodium carbonate–potassium carbonate (FNK) were carried out. The addition of Na_2CO_3 in FN was 40% and the calcination temperatures was varied from 600 °C to 1200 °C. The addition of K_2CO_3 in FK was 50% and the calcination temperatures was from 600 °C to 1100 °C. The experimental conditions of FNK are shown in Table S1.†

Acid leaching process. The acid leaching process was conducted in a three-necked flask, which was immersed in a temperature-controlled water bath and placed on a hot plate magnetic stirrer to maintain a constant temperature. As-calcined fly ash, kaliophilite and nepheline acquired after calcinating at 900 °C were used to evaluate the effect of acid leaching time and acid concentration on metal leaching efficiency and crystalline structure. The samples ground in a mortar to pass through a 100-mesh sieve. Then 40 mL of HCl solution with a concentration of 2.5% was put water bath at 25 °C before adding 2.0 g of sample. The slurry was stirred with a magnetic stirrer at 500 rpm for 2 minutes. In the leaching process, 10 mL of slurry samples were collected at selected time intervals (*i.e.*, 0.5, 1, 2, 4, 8 and 12 h). Then the solid phase was obtained by centrifugation, and then dried in a vacuum drying oven. The influence of acid treatment was monitored by the changes in XRD patterns and FT-IR spectra.

Different concentrations of HCl, ranging from 2.5% to 30%, were used to evaluate the effects on pore structure and leaching of metal ions, such as Al, Si, K, and Na. The experiments were carried out at a reaction temperature of 80 °C for 2 hours with the condensing reflux attached. Nepheline, kaliophilite and $(Na, K)AlSiO_4$ with hexagonal crystalline phase acquired after calcinating at 900 °C were used to investigate the effect of mineral phase on pore structure.

Characterization and analysis

Phase compositions and crystal structure of the samples were identified using X-ray diffraction (XRD, D2 PHASER model). The chemical composition of all samples was determined by S8 Tiger X-ray fluorescence spectrometer (XRF, Bruker, Germany). The concentrations of metal ions in leaching filtrates were measured using an inductively coupled plasma and optical emission (ICP-OES, Icap 6000 model) spectrometer. Fourier transform infrared absorption spectrometer (FTIR) was used to analyse the existence forms and surface chemical groups of aluminum and silicon in the samples, and the scanning range was 4000–100 cm^{-1}. The specific surface areas of the porous materials obtained were calculated by the Brunauer–Emmett–Teller (BET) with a relative pressure range of $0.06 < P/P_0 < 0.15$

Table 1 Chemical compositions of PC fly ash used in the study (wt%)

Components	SiO_2	Al_2O_3	TiO_2	Fe_2O_3	Na_2O	K_2O	MgO	P_2O_5	CaO	Li	Ga
Contents	45.63	43.88	1.91	2.65	—	0.43	0.22	0.33	4.95	252 ppm	68 ppm

for the adsorption isotherm. Transmission electron microscopy (TEM) images were obtained using a JEM-2100 transmission electron microscope. After leaching, the leaching efficiency (η) was calculated using the formula shown in eqn (1).

$$\eta_x = \frac{c \times V}{m \times W} \times 100\% \tag{1}$$

where η_x is the leaching efficiency of elements (Na, K, Al, Si, Li, Ga etc.) (%); c is the concentration of elements in the leaching liquor (g L^{-1}); V is the volume of leaching liquor (L); m is the mass of as-calcined fly ash (g); W is the content of elements (Na, K, Al, Si, Li, Ga etc.) in as-calcined fly ash (g g^{-1}).

Results and discussion

Mineral phase transformation

XRD analysis. Fig. S1(a)† shows the XRD patterns of raw fly ash and FN calcined at various temperatures. The mineral composition of raw fly ash mainly includes crystalline phase minerals (mullite, quartz etc.) and amorphous phase minerals (amorphous silica, glass etc.). After calcinating at 600 °C, the diffraction peaks of low temperature carnegie phase of sodium aluminosilicate (NaAlSiO$_4$, low carnegieite, orthorhombic)[26] appears. When the calcination temperature is increased to 800 °C, sodium ions (Na$^+$) enter and destroy the mullite lattice to generate new sodium aluminosilicate minerals (nepheline, hexagonal, JCPDS No. 35-0424). In the calcined FK sample, kaliophilite (KAlSiO$_4$, hexagonal, JCPDS No. 12-0134) generates at 900 °C. With the increase of temperature to 1100 °C, the

diffraction peaks of KAlSiO$_4$-O1 (KAlSiO$_4$, orthorhombic, JCPDS No. 33-0989)[27,28] (Fig. S2(a)†) are detected.

Fig. 1(a) shows the XRD patterns of FNK calcined at 900 °C with various molar ratios of Na$_2$CO$_3$/K$_2$CO$_3$. The lattice parameters of as-calcined phases in the NaAlSiO$_4$–KAlSiO$_4$ system were fitted by the GSAS method of Rietveld crystal structure refinement until the results converged[29,30] ($R_{wp} < 10\%$), and the cell parameters are shown in Table 2. The volume per formula in NaAlSiO$_4$–KAlSiO$_4$ system is shown in Fig. S3.† The 0Na–100K sample generates kaliophilite after calcination at 900 °C. Compared with the natural sample, the a-axis length of the synthesized kaliophilite (5.2 Å) is much smaller than the natural kaliophilite (26.9 Å). But it is close to the potassium silica (5.2 Å), indicating that the kaliophilite synthesized in this paper is actually more inclined to a disordered potassium silica crystal structure.[31,32] In the 25Na–75K sample, kalsilite (KAlSiO$_4$, JCPDS No. 85-1413) can be formed. With the addition of Na$_2$CO$_3$ increasing to 50%, the potassium silica crystalline structure gradually becomes complete. No relevant characteristic peaks of sodium aluminosilicate appear, indicating that Na enters the potassium aluminosilicate lattice and crystallized in the hexagonal structure. With the increase of Na$_2$CO$_3$ addition to 75%, the new diffraction peaks appear at 21.0°, 26.9° and 30.7°, which confirms the formation of (Na, K)AlSiO$_4$ (nepheline, JCPDS No. 89-8763). The a-axis and b-axis of the lattice are slightly shortened, and the c-axis changes little (as listed in Table 2), indicating that Na enters the smaller alkali crystallization sites in the crystal. The acquired sodium-potassium
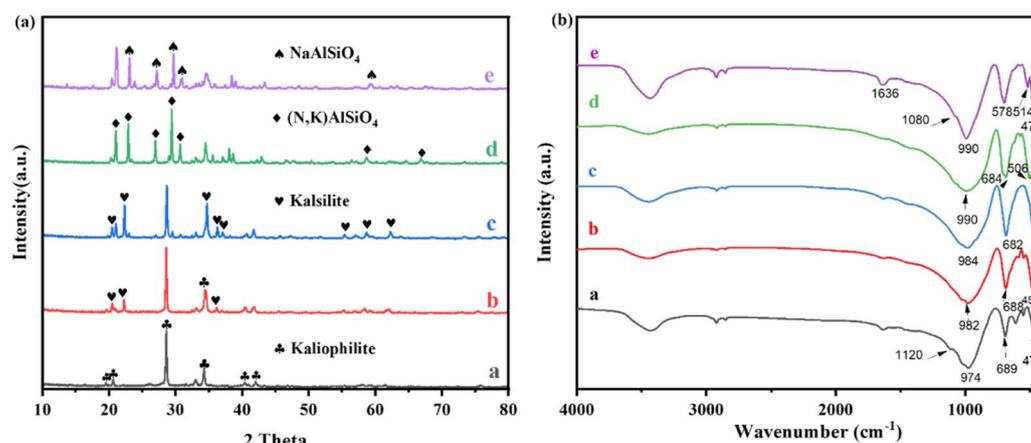

Fig. 1 XRD patterns (a) and FT-IR spectra (b) of as-calcined fly ash with Na$_2$CO$_3$–K$_2$CO$_3$ system at 900 °C (a 0Na–100K; b 25Na–75K; c 50Na–50K; d 75Na–25K; e 100Na–0K).

Table 2 Lattice parameters of each phase in NaAlSiO$_4$–KAlSiO$_4$ system

Filename	Phase	a (Å)	b (Å)	c (Å)	V (Å^3)	Z
0Na–100K	Hex	5.21070(17)	5.21070(17)	8.6022(4)	202.207(15)	2
25Na–75K	Hex	5.1846(4)	5.1846(4)	8.6482(10)	201.322(34)	2
50Na–50K	Hex	5.1408(5)	5.1408(5)	8.6066(14)	196.98(4)	2
75Na–25K	Hex	10.0724(4)	10.0724(4)	8.4165(4)	739.47(6)	8
100Na–0K	Hex	9.9589(16)	9.9589(16)	8.3327(19)	715.72(26)	8

nepheline had larger lattice parameters than sodium nepheline, which is attributed to the lattice expansion due to K ($R_K = 0.77$ Å) enters the non-skeletal cation site with different K and Na ($R_{Na} = 0.63$ Å). According to Fig. S1(a),† the coexistence of hexagonal and orthorhombic crystalline phases of sodium nepheline in the 100Na–0K sample.

FT-IR analysis. Fig. S1(b)† shows the FTIR spectra of FN samples calcined at various temperatures. At 600 °C, the sample presents characteristic peak at 694 cm^{-1} corresponding to

Fig. 2 SEM images of as-calcined fly ash with Na_2CO_3–K_2CO_3 system at 900 °C (a 0Na–100K; b 25Na–75K; c 50Na–50K; d 75Na–25K; e 100Na–0K).

irregular stretching vibrations of Si–O, which indicates the transition from Si–O–Aloct (Al octahedron) to Si–O–Altet (Al tetrahedron).[33] At 800 °C, the main absorption bands appear at 984, 694 and 472 cm^{-1}, indicating the complete transformation of aluminum octahedra to aluminum tetrahedra and the formation of structurally stable hexagonal sodium nepheline.[34] For FK samples, as shown in Fig. S2(b),† the absorption band at 976 cm^{-1} appears after calcination at 800 °C with a shoulder at 1120 cm^{-1}, indicating the complete transformation of aluminum octahedra to aluminum tetrahedra. When the calcination temperature is increased to 1100 °C, it is obvious to observe the sharper peaks at 608 and 552 cm^{-1} (Fig. S2(b)†), the phenomena can be explained the formation of $KAlSiO_4$-O1 phase.

The phase transformation of the FNK system is further analysed by FT-IR spectra as shown in Fig. 1(b). In the 0Na–100K sample, characteristic peaks including Si–O and Al–O stretching vibrations in the 600–1200 cm^{-1} range and the adsorption peaks of kaliophilite at 974, 689, 610, 550, 474 cm^{-1} could be detected. In the 25Na–75K sample, the absorption bond shifts from 974 to 982 cm^{-1}, the absorption bonds at 610 cm^{-1} and 550 cm^{-1} become weaken in intensity, indicating the skeletal TO_4 arrangement in kaliophilite tended to be ordered. In the 50Na–50K sample, it is obviously observed that the major absorption bonds formed at 984 and 682 cm^{-1}, which relates to the asymmetric and symmetric stretching vibrational of the Kalsilite and confirms the crystalline structure becomes ordered state. In the 75Na–25K sample, the shoulder peak at about 1080 cm^{-1} appears, which confirms the formation of (Na, K)$AlSiO_4$. The absorption peaks at 990, 695 and 472 cm^{-1} appear in the 100Na–0K sample, indicating the formation of sodium nepheline. In addition, the FTIR spectra of sodium nepheline split significantly compared to disordered kaliophilite because of the more ordered structure at the tetrahedral position.

Morphology. Fig. 2 shows the SEM images of as-calcined fly ash with different contents of Na_2CO_3 and K_2CO_3 at 900 °C. The microstructure of $KAlSiO_4$ with irregular flake particles can be observed from Fig. 2(a). With the increase of Na_2CO_3 content in
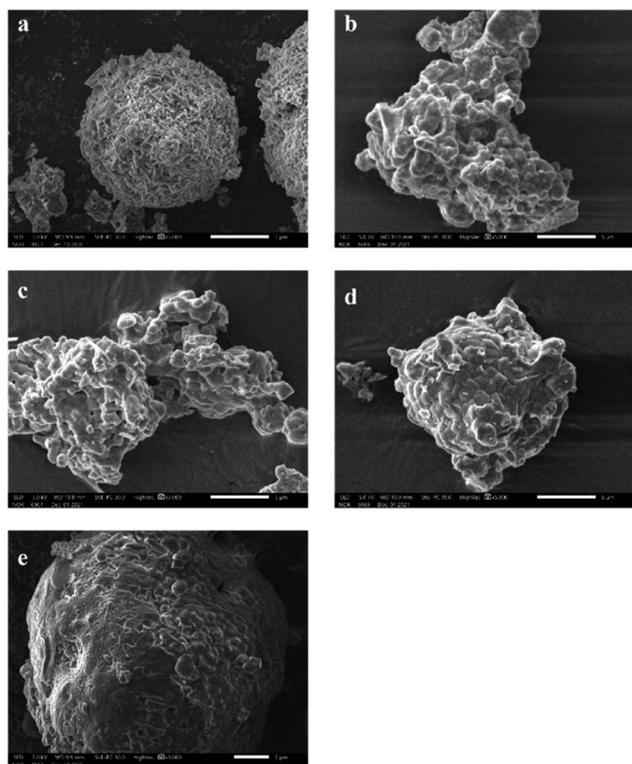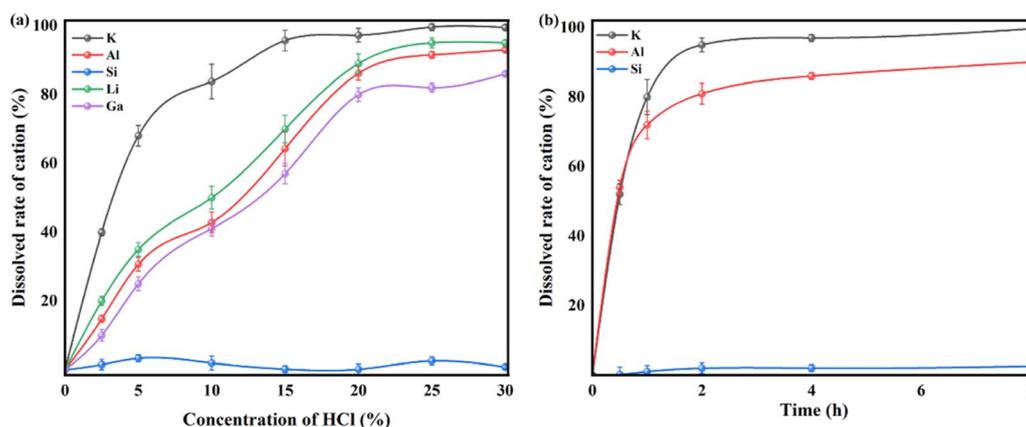

Fig. 3 Leaching efficiency of valuable metals including Si from as-calcined fly ash with K_2CO_3 with different concentration of HCl (a) solution and leaching time (b).

the mixed additives, the calcined samples shows that the geometric edges of the particles are blurred, resulting in higher degree of agglomeration and nanostructures with irregular spherical particles (Fig. 2(b) and (c)). As presented in Fig. 2(d), when the fly ash is calcined with 75Na–25K additive, a larger and more uniform nanostructure with a clearer hexagonal contour of edges is generated. It is further shown in Fig. 2(e) that the addition of Na_2CO_3 promotes the activation reaction of fly ash, resulting in the agglomeration of aluminosilicate particles formed in the calcination process, and the particle edge morphology varying from irregular to hexagonal.

Valuable metal recovery during acid leaching process

The different crystalline structures of nepheline and kaliophilite would inevitably lead to the difference of metal leaching behaviors and pore structure of silica materials. In this section, the effects of crystalline structure including kaliophilite and nepheline on metal leaching behaviors and pore formation were investigated systematically.

Kaliophilite. Fig. 3 shows the leaching efficiency of valuable metals including Si from as-calcined fly ash with K_2CO_3 with different concentration of HCl solution and leaching time. It can be found that HCl solution concentration has great influence on metal leaching behavior. With the increase of HCl solution concentration, the leaching efficiencies of all the valuable metals Al, Li, Ga and K, are increased gradually, especially for K, and keep relatively stable when the concentration is 20%. During the acid leaching process, the leaching efficiency of Si is kept low as less than 5%. The influence of leaching time demonstrating that fast dissolution of valuable metals occurs within the first hour, and basically reaches equilibrium within about 2 h of leaching. The leaching efficiencies of Al, Li, and Ga could reach 86.17%, 89% and 80%, respectively, while 97.25% leaching efficiency of K could be achieved, providing conditions for etching of crystal structure.

The influence of acid treatment on kaliophilite was monitored by the changes in XRD patterns and FT-IR spectra (Fig. 4). The reduction in intensity and the increase in the width of peak (Table S2†) indicate that the crystallinity of kaliophilite is decomposing by acid leaching. In the XRD patterns, it is clearly observed that the acid leaching makes the kaliophilite diffraction peaks intensity significantly weakened. The $I_{(102)}/I_{(002)}$ decreases with increasing acid leaching time according to Table
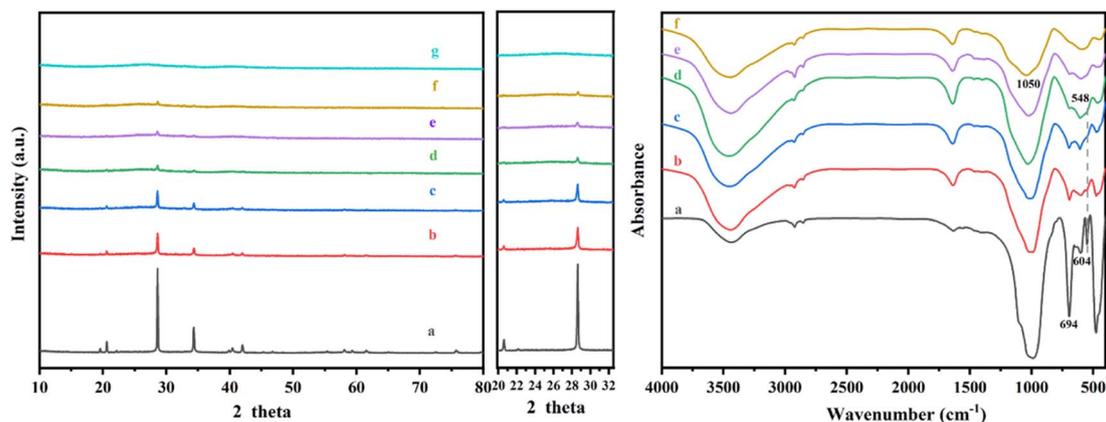

Fig. 4 XRD patterns and FTIR spectra of kaliophilite during acid etching for different time (a kaliophilite; b 0.5 h; c 1 h; d 2 h; e 4 h; f 8 h; g 12 h).
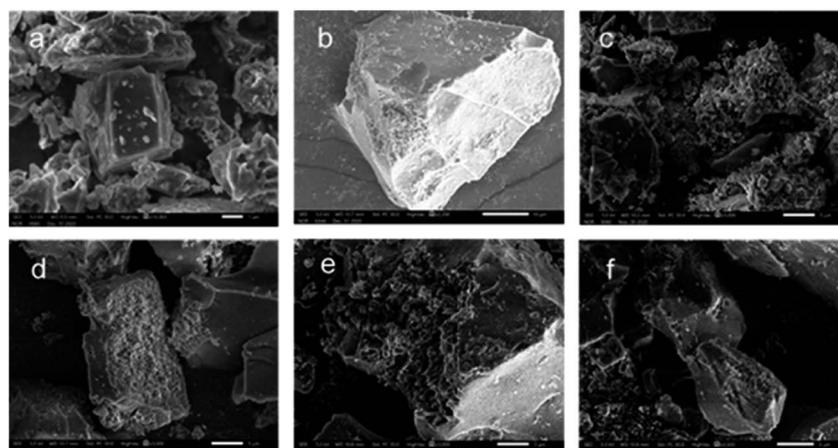

Fig. 5 SEM images of as-calcined kaliophilite with different acid etching time (a kaliophilite; b 0.5 h; c 1 h; d 2 h; e 4 h; f 8 h).
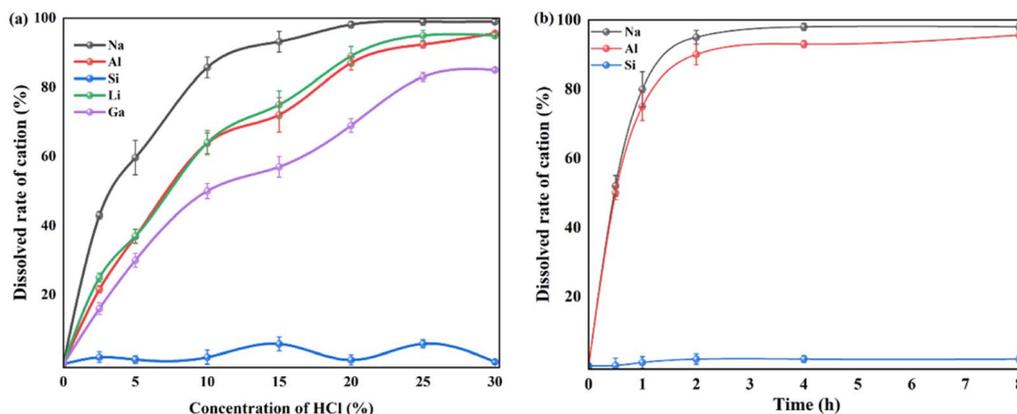
© 2024 The Author(s). Published by the Royal Society of Chemistry

Fig. 6 Leaching efficiency of valuable metals including Si from as-calcined fly ash with Na_2CO_3 with different concentration of HCl (a) solution and leaching time (b).

S2,† demonstrating that the hydrochloric acid destroys the crystal plane (002) more than (102), and the lattice of kaliophilite severely damages along the c-axis direction. As shown in Fig. 4(b), the bond at 988 cm^{-1} shown by kaliophilite is due to the asymmetric stretching vibration of the R–O–Si and the band observed at 548 cm^{-1} is due to the stretching vibrations of the Al–O. The Al–O stretching band at 548 cm^{-1} decreases slightly after treatment with HCl for 0.5 h and 1 h, while the main absorption bond at 988 cm^{-1} disappears. Acid leaching also causes the absorption bands at 988 cm^{-1} to become broadened, reflecting the amorphization of the crystalline structure. With increasing acid leaching time, the vibrational band of the Si–O near 1050 cm^{-1} shifts toward the high frequency number, confirming that the electron cloud density and the vibrational frequency of the Si–O bond increases. In this work, the intensities of all the major bands decrease due to the amorphization of the kaliophilite after acid leaching and the formation of amorphous silica.

Fig. 5 gives SEM images of as-leached samples with different acid etching time. It can be observed from Fig. 5(a) that the

unetched crystal structure is tight, and the geometric edge is clear. After acid treatment for 0.5 h (Fig. 5(b)), it can be observed that the crystal surface becomes rough. Further acid etching along the grain boundary causes the grain edge to become rough as shown in Fig. 5(c). With the acid treatment time increasing 2 h or even 4 h, the etching area and etching depth are further increased, forming corrosion pits (Fig. 5(e)). After the reaction time reaches 8 h, the corrosion pits are connected to form a series of corrosion ditches as presented in Fig. 5(f).

Nepheline. Fig. 6 presents the leaching efficiency of valuable metals including Si from as-calcined fly ash with Na_2CO_3 with different concentration of HCl solution and leaching time. It can be found that the changes of leaching efficiencies of Al, Li, Ga and Na is similar to that of as-calcined fly ash with K_2CO_3, however, the leaching efficiencies of Al, Li and Ga could reach 92.38%, 95% and 83%, respectively, while 99% of Na could be leached after acid leaching with 25% HCl solution concentration for 2 h, further confirming that as-calcined fly ash with Na_2CO_3 exhibit higher acid soluble activity than that with K_2CO_3.
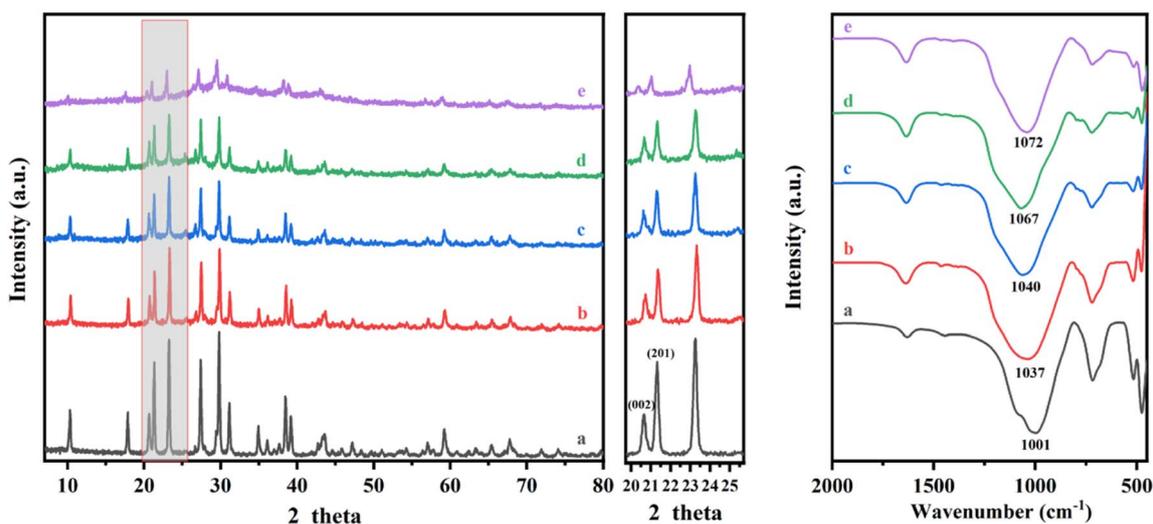

Fig. 7 XRD patterns and FTIR spectra of nepheline during acid etching for different time (a kaliophilite; b 0.5 h; c 1 h; d 2 h; e 4 h).

By comparison, the crystalline structure of nepheline during acid leaching is also investigated by XRD patterns and FTIR spectra (Fig. 7). The characteristic diffraction peaks of nepheline become weaken gradually and disappear with the prolonging of acid leaching time. To quantify the change of crystallinity structure, like kaliophilite, the crystal plane (002) at 21.315° and the crystal plane (201) at 23.180° are selected to reveal the leaching process. The value of $I_{(201)}/I_{(002)}$ is chosen to further indicate the acid leaching process (Table S3†), and the larger the value, the faster the destruction along the c-axis direction. However, the ratio of $I_{(201)}/I_{(002)}$ changes little, demonstrating that unlike kaliophilite, acid treatment would damage all the crystal planes of nepheline, not the certain crystal plane. As shown in Fig. 7, the range of 1000–1090 cm^{-1} in the FTIR spectrum represents the shape of the Si–O group absorption band. The spectrum line moves to the left continuously during the acid treatment. The absorption peak at 1037 cm^{-1} corresponding to the stretching vibration of Si (Al)–O becomes flat, indicating that nepheline still maintains a certain crystalline structure, but some amorphous phase also appears after acid treatment for 0.5 h. Due to that the asymmetric dissolution of Si and Al affected the crystal symmetry, and the electron cloud density of Si–O bond in the six membered ring increased without the contention of Al, the absorption peak continued to shift to the left, resulting in increasing the vibration frequency of Si–O bond. With the increase of acid treatment time, the absorption peak becomes sharp, implying that

the Si–O tetrahedron tends to be arranged periodically with the dissolution of Na and Al.

In situ preparation of porous silica materials

Effect of acid leaching on pore structure. The mechanism of pore formation during acid leaching is shown in Fig. S4.† During acid leaching process, Al, Na, K and Si could be leached from crystalline structure and porous silica is formed. Using different concentrations of HCl solutions as lixiviants, the leaching efficiency and pore structure of kaliophilite and nepheline were characterized. The pore structure is characterized by N$_2$ adsorption desorption isotherm and the results are shown in Fig. 8 and Table 3. As illustrated in Fig. 3, the leaching efficiency of Al and K improves as the concentration of HCl increases, the dissolution rate reaches 100% for K when using more than 15% HCl solution. After 2.5% HCl treatment, the isotherm is classified as type III according to IUPAC recommendation. The pore size distribution shows no peaks, suggesting the sample is dominated macropore with low specific surface area and large pore volume and size. After being treated with higher concentration of acid, the adsorption of N$_2$ increases significantly and the isotherms conform to type IV isotherm, indicating the presence of abundant mesopores. As illustrated by Fig. 8(b), the pore size distribution curve steepens slightly towards smaller pore sizes and shows a sharp peak at a radius of 3.40 nm when the acid concentration is 15%,
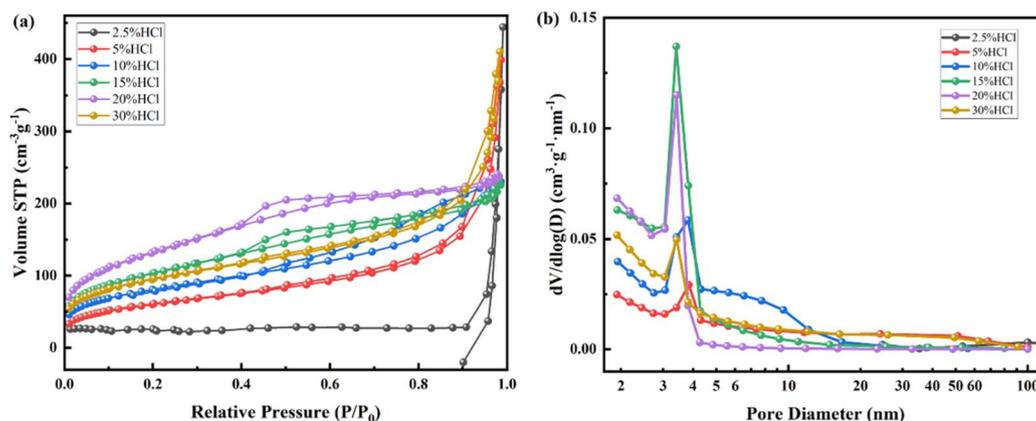

Fig. 8 N$_2$ adsorption desorption isotherm (a) and pore size distribution (b) of kaliophilite calcined at 900 °C after treatment with different concentrations of HCl (2.5–30%) at 80 °C.

Table 3 Nano pore property parameters of kaliophilite after being treated with 2.5–30% hydrochloric acid at 80 °C for 2 h

HCl (%)	S_{BET} (m^2 g^{-1})	S_{micro} (m^2 g^{-1})	S_{exter} (m^2 g^{-1})	V_{BJH} (cm^3 g^{-1})	V_{micro} (cm^3 g^{-1})	D_a (nm)	D_{BJH} (nm)	N$_2$ adsorption curve type	Hysteresis loop type	Hole shape
2.5	140.8	63.2	77.7	0.11	0.032	—	—	III	C	Wedge shape
5	215.0	14.6	200.4	0.33	0.005	6.14	3.84	IV	C	Wedge shape
10	287.0	24.9	262.1	0.33	0.010	4.55	3.81	IV	B	Plate shape
15	369.4	21.6	347.8	0.31	0.007	3.38	3.40	IV	E	Ink bottle shape
20	475.9	—	476.9	0.35	—	2.93	3.43	IV	E	Ink bottle shape
30	332.4	34.0	298.4	0.40	0.016	4.79	3.42	I + IV	C	Wedge shape

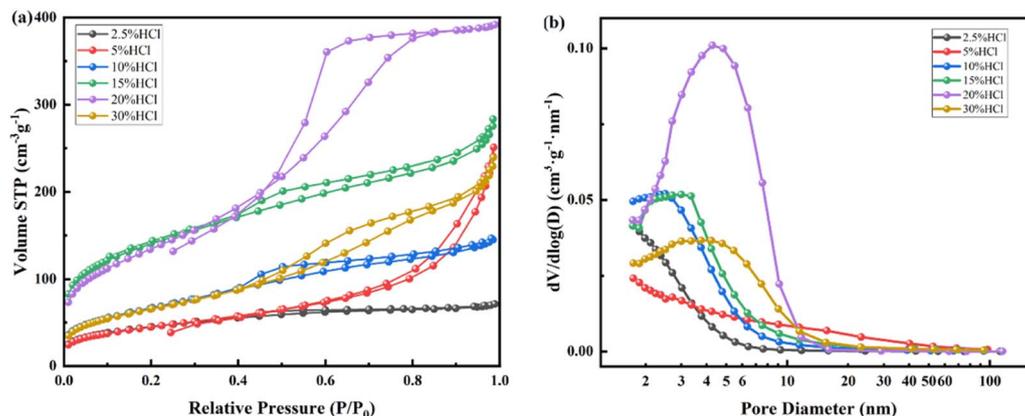**Fig. 9** N$_2$ adsorption desorption isotherm (a) and pore size distribution (b) of nepheline calcined at 900 °C after treatment with different concentrations of HCl (2.5–30%) at 80 °C.

suggesting that the macropore gradually transformed into mesopore. This phenomenon may be due to the continuous leaching of Al and K (Fig. 3), and the pore shape is mainly ink bottle. When the acid concentration is 30%, the specific surface area and pore volume decrease, but the average pore size increase, which may be ascribed to that dissolved Al adsorbs on the surface of the mesopore material and generates the large wedge shape pores.

The N$_2$ adsorption desorption isotherm and pore size distribution after acid leaching for nepheline with 2.5–30% HCl are also tested as shown in Fig. 9, and the nano pore parameters are listed in Table 4. The dissolution rate of Al, Na and Si are also shown in Fig. 5. For Na, the dissolution rate reaches 100%

when using more than 20% HCl solution. As shown in Fig. 9, like kaliophilite, the most probable pore size distribution of nepheline changes from dispersion to concentration with the increase of acid leaching degree. When the acid concentration from 2.5% to 20%, the micropores decrease and mesopores increase. When the acid concentration is 15%, the sample has the higher specific surface area, the average pore diameter and the most probable pore diameter are close, indicating that the mesoporous structure of the ink bottle is more uniform and concentrated. Na and K are almost dissolved after treatment with 20% HCl (Fig. 5). Same as kaliophilite, the sample generates the large wedge shape pores after treatment with 30% HCl. Compared to kaliophilite, the specific surface, pore volume and

Table 4 Nano pore property parameters of nepheline after being treated with 2.5–30% hydrochloric acid at 80 °C for 2 h

| HCl (%)	S_{BET} (m^2 g^{-1})	S_{micro} (m^2 g^{-1})	S_{exter} (m^2 g^{-1})	V_{BJH} (cm^3 g^{-1})	V_{micro} (cm^3 g^{-1})	D_a (nm)	D_{BJH} (nm)	N$_2$ adsorption curve type	Hysteresis loop type	Hole shape
2.5	160.6	9.42	151.1	0.10	0.003	2.61	—	III	C	Wedge shape
5	160.9	—	161.4	0.28	—	7.06	—	IV	B	Plate shape
10	242.8	—	255.5	0.11	—	3.49	2.50	IV	E	Ink bottle shape
15	491.1	75.0	416.1	0.38	0.034	3.14	3.12	IV	E	Ink bottle shape
20	490.0	—	502.1	0.60	—	4.89	4.27	IV	E	Ink bottle shape
30	239.3	34.0	248.5	0.31	0.016	5.23	3.75	IV	C	Wedge shape
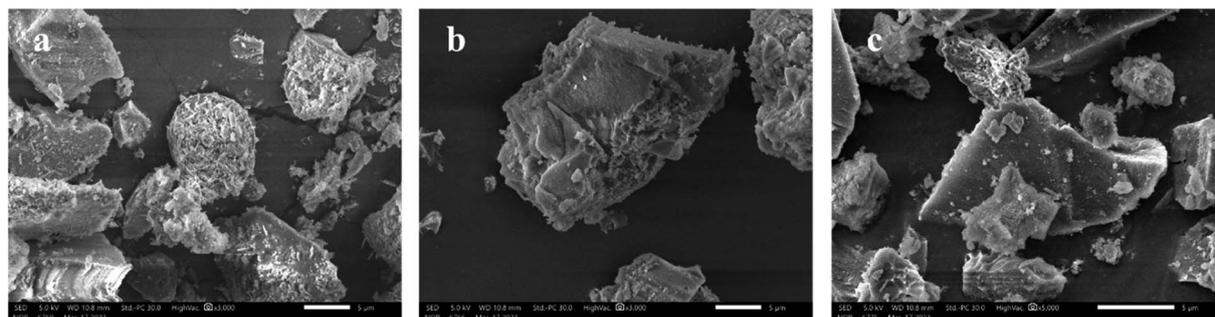
Fig. 10 SEM images of (a) MS-K, (b) MS-N and (c) MS-NK.
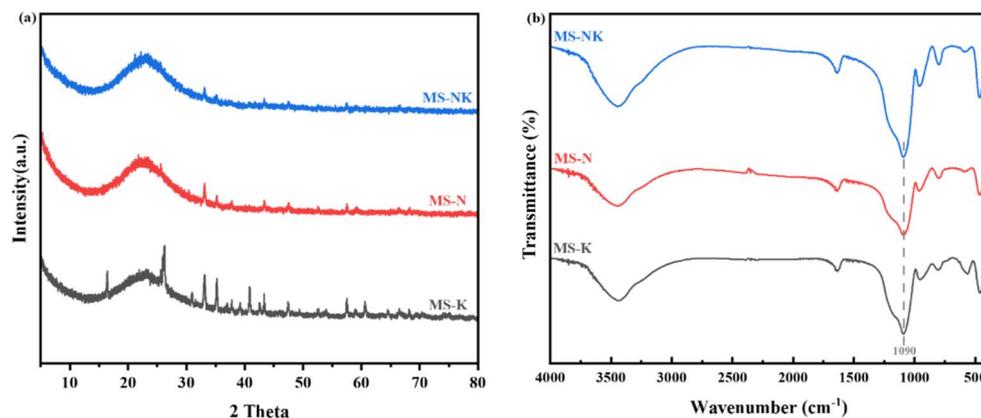
Fig. 11 XRD patterns (a) and FTIR spectra (b) of MS-K, MS-N and MS-NK.

pore diameter of nepheline are larger in the same experimental conditions, which shows that the activation degree of nepheline is higher.

Effect of mineral phase on pore structure. Kaliophilite, nepheline and (Na, K)AlSiO$_4$ with hexagonal crystalline phase are selected to evaluate the effect of mineral phases on pore structure. The three samples were treated by 20% HCl and the samples are named MS-N, MS-K and MS-NK. The SEM images of MS-N, MS-K and MS-NK are shown in Fig. 10. For MS-K, the geometric edge of crystal structure is clear and the surface is rough. Corrosion pits form on surface of MS-N. There is almost no original crystal structure for MS-NK and the surface appear corrosion ditches. The XRD patterns and FTIR spectra of MS-K, MS-N and MS-NK are shown in Fig. 11. From the XRD patterns, it can be seen that three samples have obvious bulging peaks corresponding to mesoporous silica. MS-NK has no other impurity peaks. MS-N and MS-NK still have peaks of mullite. This also indicates that the effect of co-activation Na and K is better. In the FTIR spectrum, the adsorption band of 1090 cm^{-1} represents the shape of the Si–O group. The range of 1000–800 cm^{-1} correspond to the shape of the Si–OH group absorption band.

The N$_2$ adsorption desorption isotherm and pore size distribution are shown in Fig. 12, the nano pore parameters are listed in Table 4. As depicted in Fig. 12(a), the isotherms of as-prepared samples correspond to the type IV isotherm with a hysteresis loop attributable to the H3 type, suggesting the formation of ink bottle shaped mesopores after acid leaching. Comparing with MS-K and MS-N, the N$_2$ adsorption–desorption isotherm of MS-NK is closer to the y-axis at low P/P_0 (0–0.2), suggesting the presence of abundant micropores. As shown in Fig. 12(b), the as-prepared three samples exhibit similar pore size distribution curves, suggesting the formation of mesopores after acid leaching.

As listed in Table 5, the as-prepared samples present different pore structures under the same leaching conditions. The MS-N sample has more mesopores with larger specific surface area than MS-K. The addition of Na$^+$ makes the arrangement of skeletal silica–alumina tetrahedra more orderly and the space symmetry of crystal is higher, so as-prepared sample from nepheline has more mesopores and pore size distribution is more uniform. The MS-NK sample possesses higher specific surface area (746.76 m^2 g^{-1}) and pore volume (0.48 cm^3 g^{-1}) than MS-N and MS-K, which is consistent with
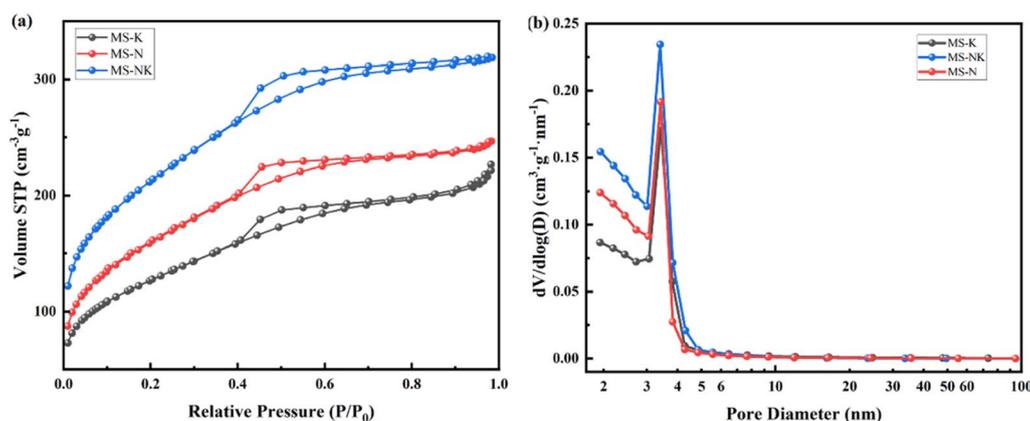

Fig. 12 N$_2$ adsorption desorption isotherms (a) and pore size distribution (b) of kaliophilite (MS-K), nepheline (MS-N) and (Na, K)AlSiO$_4$ (MS-NK) with hexagonal phase after acid treatment (20% HCl–80 °C–2 h).

Table 5 Nano pore property parameters of kaliophilite, nepheline and (Na, K)AlSiO$_4$ after acid treatment (20% HCl–80 °C–2 h)

Sample	S_{BET} (m^2 g^{-1})	S_{micro} (m^2 g^{-1})	S_{exter} (m^2 g^{-1})	V_{BJH} (cm^3 g^{-1})	V_{micro} (cm^3 g^{-1})	D_a (nm)	D_{BJH} (nm)
MS-K	448.02	36.35	411.66	0.32	0.01626	2.88	3.42
MS-N	565.54	25.71	539.83	0.37	0.09913	2.63	3.41
MS-NK	746.76	66.92	679.84	0.48	0.03087	2.61	3.39

the N$_2$ adsorption desorption isotherm and pore size distribution. In the aluminosilicate structure, the introduction of different cations significantly changes structural environment of the framework. After Na$^+$, K$^+$, and Na/K introducing, the ⟨Al–O⟩ average bond lengths are 1.805 Å, 1.746 Å, and 1.717 Å, respectively. Na promotes the dissolution of skeleton Al more easily than K, resulting in more concentrated pore size distribution of as-etched sample.

Recovery process

In this paper, novel process *via* mineral phase transformation and acid leaching for high value utilization of fly ash was explored, which realized the recovery of valuable metal elements and controllable preparation of porous silica. The recovery process of leachate and residue from high-alumina fly ash is shown in Fig. 13. The as-calcined FN, FK and FNK generate nepheline, kaliophilite and (Na, K)AlSiO$_4$, respectively. By acid leaching, the high dissolution efficiency of Al, Li, Ga besides Na and/or K could be realized, while Si hardly dissolves. During the leaching process, about 85.0% of Al, and more than 80.0% of Li and Ga could be leached in the leaching liquors, providing conditions for the recovery of Al, Li and Ga. After acid leaching, Si is basically in leaching residue with rich pore structure, and the pore structure of porous silica could be controlled by mineral phase transformation and acid leaching conditions. The porous silica materials can be used in adsorption or carrier of composite phase change materials. In the previous work, comprehensive utilization of leaching liquors containing Al, Li, Ga *etc.* can be realized, and crystalline aluminum chloride and sodium chloride can be recovered through evaporation concentration and crystallization.[35]

Fig. 13 The recovery process of leachate and residue from high-alumina fly ash.

Furthermore, Li could be recovered as Li$_2$CO$_3$ by solvent extraction and carbonation,[36] while Ga could be recovered by selective adsorption.[37] In conclusion, this paper provides a novel pathway for comprehensive and high value utilization of Al, Si, Li, Ga *etc.* in coal fly ash.

Conclusions

Full recycling to high value-added products from coal fly ash could be achieved by the developed process in this paper. Recovery of valuable metals including Al, Li and Ga and *in situ* preparation of porous silica materials for high value utilization of fly ash could be successfully realized.

(1) Mineral phase transformation of stable mullite, quartz is the key technology for full utilization of fly ash. With the addition of Na, sodium induced the conversion of disordered potassium feldspar to potassium silica, while the addition of potassium induced the conversion of the orthorhombic phase of sodium nepheline to the hexagonal phase. Compared with single auxiliary activation, the co-activation of mullite by Na and K formed a composite nepheline structure of Na and K. The mullite reaction in the system was more complete, and the amount of activator was reduced.

(2) During the acid leaching process, Al, Li, and Ga could be leached with the efficiencies of 86.17%, 89%, and 80% in FK system. In the FN system, the efficiencies of Al, Li, and Ga are 92.38%, 95%, and 83%, respectively. The leaching liquors can be used to produce crystal aluminum chloride, lithium carbonate and gallium. The acid leaching caused destruction to the crystal structure of kaliophilite and nepheline. For kaliophilite, the hydrochloric acid destroyed the crystal plane (002) more than (102), and the lattice of KAlSiO$_4$ was severely damaged along the *c*-axis direction. For nepheline, acid treatment would damage all the crystal planes of nepheline, not the certain crystal plane.

(3) The acid concentration has significant effects on the pore shape and pore size of the products. It is the same for kaliophilite and nepheline that the change order of pore shape was: no mesopore, wedge, flat plate, ink bottle and wedge with the concentration of HCl increase. The higher activation degree of nepheline could produce porous silica with larger specific surface area under the same acid leaching conditions than those of kaliophilite. The products obtained from (Na, K)AlSiO$_4$ after acid leaching presents higher specific surface area (746.76 m^2 g^{-1}) and pore volume (0.48 cm^3 g^{-1}).

Conflicts of interest

The authors declare no conflicts of interest.
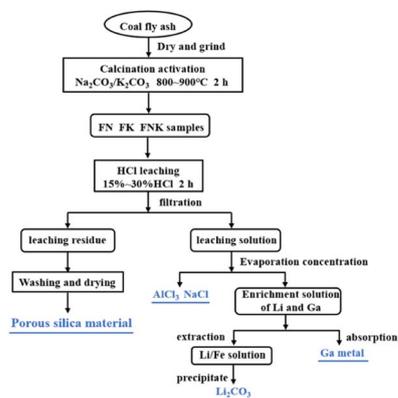
Acknowledgements

Notes and references

1 P. Liu, X. Gu, Z. Zhang, J. Rao, J. Shi, B. Wang and L. Bian, Capric Acid Hybridizing Fly Ash and Carbon Nanotubes as a Novel Shape-Stabilized Phase Change Material for Thermal Energy Storage, *ACS Omega*, 2019, **4**, 14962–14969.

2 S. Wang, Y. Zhang, Y. Gu, J. Wang, Z. liu, Y. Zhang, Y. Cao, C. E. Romero and W.-p. Pan, Using modified fly ash for mercury emissions control for coal-fired power plant applications in China, *Fuel*, 2016, **181**, 1230–1237.

3 D. H. Vu, K.-S. Wang, J.-H. Chen, B. X. Nam and B. H. Bac, Glass–ceramic from mixtures of bottom ash and fly ash, *Waste Manage.*, 2012, **32**, 2306–2314.

4 L. Wang, H. Sun, Z. Sun and E. Ma, New technology and application of brick making with coal fly ash, *J. Mater. Cycles Waste Manage.*, 2016, **18**, 763–770.

5 M. Hermassi, C. Valderrama, O. Font, N. Moreno, X. Querol, N. H. Batis and J. L. Cortina, Phosphate recovery from aqueous solution by K-zeolite synthesized from fly ash for subsequent valorisation as slow release fertilizer, *Sci. Total Environ.*, 2020, **731**, 139002.

6 T. Zhou, B. Wang, Z. Dai, X. Jiang and Y. Wang, Organotemplate-free synthesis of MOR zeolite from coal fly ash through simultaneously effective extraction of Si and Al, *Microporous Mesoporous Mater.*, 2021, **314**, 110872.

7 B. Gutiérrez, C. Pazos and J. Coca, Recovery of gallium from coal fly ash by a dual reactive extraction process, *Waste Manage. Res.*, 1997, **15**, 371–382.

8 J. Ibáñez, O. Font, N. Moreno, J. J. Elvira, S. Alvarez and X. Querol, Quantitative Rietveld analysis of the crystalline and amorphous phases in coal fly ashes, *Fuel*, 2013, **105**, 314–317.

9 O. Font, N. Moreno, X. Querol, M. Izquierdo, E. Alvarez, S. Diez, J. Elvira, D. Antenucci, H. Nugteren, F. Plana, A. López, P. Coca and F. G. Peña, X-ray powder diffraction-based method for the determination of the glass content and mineralogy of coal (co)-combustion fly ashes, *Fuel*, 2010, **89**, 2971–2976.

10 J. Zhang, S. Li, H. Li, Q. Wu, X. Xi and Z. Li, Preparation of Al–Si composite from high-alumina coal fly ash by mechanical–chemical synergistic activation, *Ceram. Int.*, 2017, **43**, 6532–6541.

11 J. E. Nyarko-Appiah, W. Yu, P. Wei, W. Jiang, Z. Liang and S. Gong, The alumina enrichment and Fe-Si alloy recovery from coal fly ash with the assistance of Na_2CO_3, *Fuel*, 2022, **310**, 122434.

12 N. Yuan, X. Zhang, A. Zhao, K. Tan and Y. Cui, High-alumina fly ash as sustainable aluminum sources for the in situ preparation of Al-based eco-MOFs, *Colloids Surf., A*, 2022, **640**, 128421.

13 J. Fan, G. Wang, Q. Li, H. Yang, S. Xu, J. Zhang, J. Chen and R. Wang, Extraction of tellurium and high purity bismuth from processing residue of zinc anode slime by sulfation roasting-leaching-electrodeposition process, *Hydrometallurgy*, 2020, **194**, 105348.

14 X. Li, H. Wang, Q. Zhou, T. Qi, G. Liu and Z. Peng, Efficient separation of silica and alumina in simulated CFB slag by reduction roasting-alkaline leaching process, *Waste Manage.*, 2019, **87**, 798–804.

15 M. Izquierdo and X. Querol, Leaching behaviour of elements from coal combustion fly ash: An overview, *Int. J. Coal Geol.*, 2012, **94**, 54–66.

16 J. Li, J.-M. Gao, Y. Guo and F. Cheng, Energy-efficient leaching process for preparation of aluminum sulfate and synergistic extraction of Li and Ga from circulating fluidized bed fly ash, *Energy Sources, Part A*, 2022, **44**, 4398–4410.

17 J.-H. Park, J.-H. Eom, S.-L. Lee, S.-W. Hwang, S.-H. Kim, S.-W. Kang, J.-J. Yun, J.-S. Cho, Y.-H. Lee and D.-C. Seo, Exploration of the potential capacity of fly ash and bottom ash derived from wood pellet-based thermal power plant for heavy metal removal, *Sci. Total Environ.*, 2020, **740**, 140205.

18 N. Yuan, A. Zhao, Z. Hu, K. Tan and J. Zhang, Preparation and application of porous materials from coal gasification slag for wastewater treatment: A review, *Chemosphere*, 2022, **287**, 132227.

19 N. Yuan, H. Cai, T. Liu, Q. Huang and X. Zhang, Adsorptive removal of methylene blue from aqueous solution using coal fly ash-derived mesoporous silica material, *Adsorpt. Sci. Technol.*, 2019, **37**, 333–348.

20 Y. Mei, Q. Zhang, Z. Wang, S. Gao and Y. Fang, Novel re-utilization of high-temperature catalytic gasification ash with sodium recovery, aluminum extraction, aragonite and mesoporous SiO_2 synthesis, *Fuel*, 2023, **331**, 125727.

21 X. Zhang, Z. Huang, B. Ma, R. Wen, X. Min, Y. Huang, Z. Yin, Y. Liu, M. Fang and X. Wu, Preparation and performance of novel form-stable composite phase change materials based on polyethylene glycol/White Carbon Black assisted by super-ultrasound-assisted, *Thermochim. Acta*, 2016, **638**, 35–43.

22 Z.-Y. Zhang, X.-c. Qiao and J. Yu, Microwave selective heating-enhanced reaction rates for mullite preparation from kaolinite, *RSC Adv.*, 2014, **4**, 2640–2647.

23 L. S. Cividanes, T. M. B. Campos, L. A. Rodrigues, D. D. Brunelli and G. P. Thim, Review of mullite synthesis routes by sol–gel method, *J. Sol-Gel Sci. Technol.*, 2010, **55**, 111–125.

24 B. Wang, Y. Zhou, L. Li and Y. Wang, Preparation of amidoxime-functionalized mesoporous silica nanospheres (ami-MSN) from coal fly ash for the removal of U(VI), *Sci. Total Environ.*, 2018, **626**, 219–227.

25 C. Wang, Z. Cai, T. Wang and K. Chen, Preparation and thermal properties of shape-stabilized 1, 8-octanediol/SiO$_2$ composites *via* sol gel methods, *Mater. Chem. Phys.*, 2020, **250**, 123041.

26 Y. Kubo, G. Yamaguchi and K. Komei, Inverted phase relation in the formation of nepheline and carnegieite from the system kaolinite—sodium carbonate, *Am. Mineral.*, 1966, **51**, 516–521.

27 Y. Kubo, G. Yamaguchi and K. Kasahara, Inverted phase relation in the formation of nepheline and carnegieite from the system kaolinite—sodium carbonate, *Am. Mineral.*, 1966, **51**, 516–521.

28 L. P. Cook, R. S. Roth, H. S. Parker and T. Negas, The system K$_2$O-Al$_2$O$_3$-SiO$_2$; Part 1, Phases on the KAlSiO$_4$-KAlO$_2$ join, *Am. Mineral.*, 1977, **62**, 1180–1190.

29 I. Hassan, S. M. Antao and J. B. Parise, Cancrinite: crystal structure, phase transitions, and dehydration behavior with temperature, *Am. Mineral.*, 2006, **91**, 1117–1124.

30 K. Chow, W. A. Phillips and A. I. Bienenstock, in *Phase Transitions–1973*, ed. H. K. Henisch, R. Roy and L. E. Cross, Pergamon, 1973, pp. 333–343, DOI: 10.1016/B978-0-08-017955-1.50034-8.

31 C. Capobianco and M. Carpenter, Thermally induced changes in kalsilite (KAlSiO$_4$), *Am. Mineral.*, 1989, **74**, 797–811.

32 Y. Okamoto, A. Kawahara, Interpretation of the Crystad Structure of Synthetic Kaliophilite from the Domain Structure of Kalsilite, *Earth Science Report*, Okayama University, 1996.

33 M. Mahloujifar and M. Mansournia, Kaolinite fusion in carbonate media: KAlSiO$_4$-NaAlSiO$_4$ phase transformations and morphological study, *Mater. Res. Express*, 2019, **6**, 025040.

34 S. Markovic, V. Dondur and R. Dimitrijevic, FTIR spectroscopy of framework aluminosilicate structures: carnegieite and pure sodium nepheline, *J. Mol. Struct.*, 2003, **654**, 223–234.

35 H. Cheng, L. Wu, J. Zhang, H. Lv, Y. Guo and F. Cheng, Experimental investigation on the direct crystallization of high-purity AlCl$_3$·6H$_2$O from the AlCl$_3$-NaCl-H$_2$O(-HCl-C$_2$H$_5$OH) system, *Hydrometallurgy*, 2019, **185**, 238–243.

36 L. Cui, S. Li, J. Kang, C. Yin, Y. Guo, H. He and F. Cheng, A novel ion-pair strategy for efficient separation of lithium isotopes using crown ethers, *Sep. Purif. Technol.*, 2021, **274**, 118989.

37 Z. Zhao, L. Cui, Y. Guo, J. Gao, H. Li and F. Cheng, A stepwise separation process for selective recovery of gallium from hydrochloric acid leach liquor of coal fly ash, *Sep. Purif. Technol.*, 2021, **265**, 118455.